SUPPLEMENTARY INFORMATION

Understanding the resolution and sensitivity in photothermal nanoscale chemical imaging - a point spread function approach

Yide Zhang, Ufuk Yilmaz, Gustavo Vinicius Bassi Lukasievicz, Liam O'Faolain, Bernhard Lendl, and Georg Ramer*

E-mail:

Y. Zhang, U. Yilmaz, G. V. B. Lukasievicz, B. Lendl, G. Ramer

Institute of Chemical Technologies and Analytics, TU Wien, Getreidemarkt 9 /E164-02-1, Vienna, 1060,Austria

Email Address: georg.ramer@tuwien.ac.at

Y. Zhang, L. O'Faolain

Centre for Advanced Photonics and Process Analysis, Munster Technological University,Rossa Avenue, Bishopstown, Cork, T12P928, Ireland

G. V. B. Lukasievicz

Department of Physics, Universidade Tecnológica Federal do Paraná, Medianeira PR 85884-000, Brazil

S1 Heat equation in cylindrical coordinates

We consider the laser energy is initially absorbed by absorber according to absorption coefficient. Therefore, heat is generated internally throughout the solid absorber at a rate of $g(r, z, t)$ per unit volume (W/m^3).

The time dependent heating source term can be expressed as

$$g(r, z, t) = g_V(r, z) * \prod\left(\frac{t}{t_p}\right) \tag{S1}$$

where $\prod\left(\frac{t}{t_p}\right)$ is the rectangular box function of length t_p. $g_V(r, z)$ is the product of the optical absorption coefficient and the optical fluence

$$g_V(r, z) = \mu_a \cdot P/A_f \tag{S2}$$

where μ_a is the optical absorption coefficient, P is the excitation laser power and A_f is the optical fluence area. The sample is coated on a semi-infinite thick substrate, and covered by dry air.

The whole system can be treated as either a semi-infinite body over the domain $0 < r < \infty$ or a finite body with a radius of R_{mat}, provided that R_{mat} is sufficiently large enough to contains all possible mode solutions. The system is described by Fourier's law with the following initial conditions (IC) and boundary conditions (BC):

$$\frac{\partial^2 T(r, z, t)}{\partial r^2} + \frac{1}{r}\frac{\partial T(r, z, t)}{\partial r} + \frac{\partial^2 T(r, z, t)}{\partial z^2} + \frac{g(r, z, t)}{\kappa} = \frac{1}{\alpha}\frac{\partial T(r, z, t)}{\partial t} \quad in \quad t \geq 0 \tag{S3}$$

With boundary conditions

$$\begin{aligned}
&BC1: \quad \frac{\partial T(r,z,t)}{\partial r} = 0 \quad at \quad r = 0 \qquad \text{(symmetry)} \\
&BC2: \quad T(r = R_{mat}, z, t) = 0 \\
&BC3: \quad T(r, z = 0, t) = 0 \qquad \text{(substrate is perfect heat sink)} \\
&BC4: \quad \frac{\partial T(r,z,t)}{\partial z} = 0 \quad at \quad z = h_{mat} \quad \text{(air is insulating)} \\
&IC: \quad T(r, z, t = 0) = F(r, z)
\end{aligned} \tag{S4}$$

t is time, r is the radial distance, κ is the thermal conductivity. In the following, we take room temperature as zero, T is variant above room temperature. α is the thermal diffusivity defined as:

$$\alpha = \frac{\kappa}{\rho C_p} \tag{S5}$$

where ρ is the density and C_p is the specific heat capacity. Note: BC1 is the symmetry condition, BC2 implies that the sample is a finite cylinder with a constant temperature at the sides. This BC was chosen over the alternative option of a semi-infinite sample because it allows for a solution that is easier to handle analytically. If R_{mat} is large enough the solutions are almost identical. BC3 and BC4 indicate that the sample is finite in z direction with a constant temperature at sample/substrate interface and insulation condition at top sample/air interface.

To determine the desired Green's function, we consider the homogeneous version of the problem defined above, which we will denote as $\Psi(r, z, t)$, for the same region:

$$\frac{\partial^2 \Psi(r,z,t)}{\partial r^2} + \frac{1}{r}\frac{\partial \Psi(r,z,t)}{\partial r} + \frac{\partial^2 \Psi(r,z,t)}{\partial z^2} = \frac{1}{\alpha}\frac{\partial \Psi(r,z,t)}{\partial t} \quad in \quad 0 \le r \le R_{mat}, 0 \le z \le h_{mat} \tag{S6}$$

Now, with all homogeneous boundary conditions, we split our solution into three independent functions

$$\Psi(r, z, t) = R(r)Z(z)\Gamma(t) \tag{S7}$$

which after substitution into equation S6 yields,

$$\frac{1}{R}\left(\frac{d^2R}{dr^2}+\frac{1}{r}\frac{dR}{dr}\right)+\frac{1}{Z}\frac{d^2Z}{dz^2}=\frac{1}{\alpha\Gamma}\frac{d\Gamma}{dt}=-\lambda^2 \tag{S8}$$

Solution of separated ODE in the t dimension yields the expected form

$$\Gamma(t)=C_1e^{-\alpha\lambda^2t} \tag{S9}$$

with the remaining terms of equation S8 yielding

$$\frac{1}{R}\left(\frac{d^2R}{dr^2}+\frac{1}{r}\frac{dR}{dr}\right)+\lambda^2=-\frac{1}{Z}\frac{d^2Z}{dz^2}=\eta^2 \tag{S10}$$

Solution of the z-dimension ODE yields the desired solution form

$$Z(z)=C_2\cos\eta z+C_3\sin\eta z \tag{S11}$$

Applying BC3 yields constant $C_2=0$, while applying BC4 yields the eigenvalues for integer values of n

$$\eta=\frac{\pi}{2h_{mat}}(2n+1),\quad n=0,1,2,... \tag{S12}$$

We now consider the remaining r terms of equation S10, where we first let $\beta^2=\lambda^2-\eta^2$, and then multiply both sides by function R, yielding

$$\frac{d^2R}{dr^2}+\frac{1}{r}\frac{dR}{dr}+\beta^2R=0 \tag{S13}$$

This is the Bessel equation of order zero, and the elementary solutions are[S1]

$$R(r)=C_4J_0(\beta r)+C_5Y_0(\beta r) \tag{S14}$$

where $J_0(\beta r)$ and $Y_0(\beta r)$ are Bessel functions of order zero. The requirement of symmetry condition stated by BC1 eliminates the $Y_0(\beta r)$ term, while BC2 then yields

$$C_4 J_0(\beta_m R_{mat}) = 0 \quad for \quad m = 0, 1, 2, 3, .. \tag{S15}$$

Now λ_{nm} is,

$$\lambda_{nm}^2 = \beta_m^2 + \eta_n^2 \tag{S16}$$

having defined the eigenvalues and eigenfunctions for both spatial dimensions, we form a product solution of the separated functions and sum over all possible solutions, yielding

$$\Psi(r, z, t) = \sum_{n=0}^{\infty} \sum_{m=0}^{\infty} C_{nm} J_0(\beta_m r) sin(\eta_n z) e^{-\alpha \lambda_{nm}^2 t} \tag{S17}$$

The initial condition applied yielding

$$\Psi(t = 0) = F(r, z) = \sum_{n=0}^{\infty} \sum_{m=0}^{\infty} C_{nm} J_0(\beta_m r) sin(\eta_n z) \tag{S18}$$

To find the Fourier coefficients, we use the property of orthogonality of our two enigenfunctions over their respective intervals by applying successively the following operators to both sides of Eq. S18:[S2]

$$* \int_{z=0}^{h_{mat}} sin(\eta_i z) dz \quad and * \int_{r=0}^{R_{mat}} r J_0(\beta_j r) dr \tag{S19}$$

which yields,

$$C_{nm} = \frac{\int_{z=0}^{h_{mat}} \int_{r=0}^{R_{mat}} F(r, z) r J_0(\beta_m r) sin(\eta_n z) dr dz}{\int_{z=0}^{h_{mat}} \int_{r=0}^{R_{mat}} r J_0^2(\beta_m r) sin^2(\eta_n z) dr dz} \tag{S20}$$

The solution of the integrals in the denominator are[S1]

$$\int_{r=0}^{R_{mat}} r J_0(\beta_m r) dr = \frac{R_{mat}}{\beta_m} J_1(\beta_m R_{mat}) \tag{S21}$$

$$\int_{r=0}^{R_{mat}} r J_0^2(\beta_m r) dr = \frac{R_{mat}^2}{2} J_1^2(\beta_m R_{mat}) \tag{S22}$$

$$\int_{z=0}^{h_{mat}} sin^2(\eta_n z)dz = \frac{h_{mat}}{2} \tag{S23}$$

The solution in our general form, introducing the Fourier constants, namely,

$$\begin{aligned}\Psi(r,z,t) = &\sum_{n=0}^{\infty}\sum_{m=0}^{\infty}\frac{4J_0(\beta_m r)sin(\eta_n z)e^{-\alpha\lambda_{nm}^2 t}}{h_{mat}R_{mat}^2 J_1^2(\beta_m R_{mat})} \\ &\times\int_{z'=0}^{h_{mat}}\int_{r'=0}^{R_{mat}} F(r',z')r'J_0(\beta_m r')sin(\eta_n z')dr'dz'\end{aligned} \tag{S24}$$

We now reformulate the above solution into

$$\begin{aligned}\Psi(r,z,t) = &\int_{z'=0}^{h_{mat}}\int_{r'=0}^{R_{mat}}\left[\sum_{n=0}^{\infty}\sum_{m=0}^{\infty}\frac{4J_0(\beta_m r)sin(\eta_n z)e^{-\alpha\lambda_{nm}^2 t}}{h_{mat}R_{mat}^2 J_1^2(\beta_m R_{mat})}J_0(\beta_m r')sin(\eta_n z')\right] \\ &\times F(r',z')r'dr'dz'\end{aligned} \tag{S25}$$

The solution of the homogeneous problem S6 in terms of Green's function is given as

$$\Psi(r,z,t) = \int_{z'=0}^{L}\int_{r'=0}^{b} G(r,z,t|r',z',t')|_{t'=0}F(r',z')r'dr'dz' \tag{S26}$$

By comparing this solution with equation S24, we readily conclude that $G(r,z,t|r',z',t')|_{t'=0}$ is given by

$$G(r,z,t|r',z',t')|_{t'=0} = \sum_{n=0}^{\infty}\sum_{m=0}^{\infty}\frac{4J_0(\beta_m r)sin(\eta_n z)}{h_{mat}R_{mat}^2 J_1^2(\beta_m R_{mat})}J_0(\beta_m r')sin(\eta_n z')e^{-\alpha\lambda_{nm}^2 t} \tag{S27}$$

Green's function $G(r,z,t|r',z',t')$ is now determined by replacing t with $t-t'$, yielding the result[S2]

$$G(r,z,t|r',z',t') = \sum_{n=0}^{\infty}\sum_{n=0}^{\infty}\sum_{m=0}^{\infty}\frac{4J_0(\beta_m r)sin(\eta_n z)}{h_{mat}R_{mat}^2 J_1^2(\beta_m R_{mat})}J_0(\beta_m r')sin(\eta_n z')e^{-\alpha\lambda_{nm}^2 (t-t')} \tag{S28}$$

Then the solution of the non-homogeneous problem of equation (S3) in terms of the above Greens's function is given, according to equation (S28) as[S2]

$$
\begin{aligned}
T(r,z,t) = & \int_{z'=0}^{h_{mat}} \int_{r'=0}^{R_{mat}} G(r,z,t|r',z',t')|_{t'=0} F(r',z') r' dr' dz' \\
& + \frac{\alpha}{\kappa} \int_{t'>0}^{t} \int_{z'=0}^{h_{mat}} \int_{r'=0}^{R_{mat}} G(r,z,t|r',z',t') g(r',z',t') r' dr' dz' \\
& - \alpha \int_{t'=0}^{t} \int_{z'=0}^{h_{mat}} \left[r' \frac{\partial' G(r,z,t|r',z',t')}{\partial r'} \right]_{r'=b} f(t') dt' \\
& + \alpha \int_{t'=0}^{t} \int_{r'=0}^{R_{mat}} \left[r' \frac{\partial' G(r,z,t|r',z',t')}{\partial z'} \right]_{z'=0} f(t') dt' \\
& - \alpha \int_{t'=0}^{t} \int_{r'=0}^{R_{mat}} \left[r' \frac{\partial' G(r,z,t|r',z',t')}{\partial z'} \right]_{z'=h_{mat}} f(t') dt'
\end{aligned}
\tag{S29}
$$

where $f(t)$ is a prescribed temperature maintained at the boundaries. In our case, the medium is initially at room temperature with zero temperature variation, and temperature at boundary is not maintained. So $F(r,z) = 0$, $f(t) = 0$, then the solution of the non-homogeneous problem defined by equation (S3) is given in terms of the Green's function becomes in variable form:

$$
T(r,z,t) = \frac{\alpha}{\kappa} \int_{t'>0}^{t} \int_{z'=0}^{h_{mat}} \int_{r'=0}^{R_{mat}} G(r,z,t|r',z',t') g(r',z',t') r' dr' dz' \tag{S30}
$$

Introducing the Green's function of equation (S28) into equation (S30). We define the heat source as

$$
g(r',z',t') = g_V(r',z') * \prod (\frac{t'}{t_p}), \quad in \quad 0 \le r' \le a, z_0 - R_{abs} \le z' \le z_0 + R_{abs}, t \ge 0 \tag{S31}
$$

Substitution of the above equation and Green's function S28 into equation S30 yielding the overall temperature solution

$$
\begin{aligned}
T(r,z,t) =& \frac{\alpha}{\kappa}\int_{t'=0}^{t_p}\int_{z'=z_0-R_{abs}}^{z_0+R_{abs}}\int_{r'=0}^{R_{abs}}\sum_{n=0}^{\infty}\sum_{m=0}^{\infty}\frac{4J_0(\beta_m r)sin(\eta_n z)}{h_{mat}R_{mat}^2 J_1^2(\beta_m R_{mat})} \\
&\times r' J_0(\beta_m r')sin(\eta_n z')e^{-\alpha\lambda_{nm}^2(t-t')}g_V(r',z')\prod(\frac{t'}{t_p})dr'dz'dt' \\
=& \sum_{n=0}^{\infty}\sum_{m=0}^{\infty}A(\beta_m,\eta_n)J_0(\beta_m r)sin(\eta_n z)\begin{cases} 1-e^{-\alpha\lambda_{nm}^2 t} & \text{in} \quad 0\le t\le t_p \\ \\ (e^{\alpha\lambda_{nm}^2 t_p}-1)e^{-\alpha\lambda_{nm}^2 t} & \text{for} \quad t>t_p \end{cases}
\end{aligned}
\tag{S32}
$$

where $A(\beta_m,\eta_n)=\frac{8R_{abs}g_V}{\kappa h_{mat}R_{mat}^2}\frac{J_1(\beta_m R_{abs})sin(\eta_n z_0)sin(\eta_n R_{abs})}{J_1^2(\beta_m R_{mat})\lambda_{nm}^2\beta_m\eta_n}$. While until now, we only consider a single pulse, to model the pulse chain, we set parameter of laser repetition rate as f_{rep}, therefore, a single pulse period is $1/f_{rep}$. Eq. S32 can be modified as

$$
\begin{aligned}
T(r,z,t) =& \sum_{N=1}^{\infty}\sum_{n=0}^{\infty}\sum_{m=0}^{\infty}A(\beta_m,\eta_n)J_0(\beta_m r)sin(\eta_n z) \\
&\times\begin{cases} 1-e^{-\alpha\lambda_{nm}^2(t-\frac{1}{f_{rep}}(N-1))} & \text{in} \quad \frac{1}{f_{rep}}(N-1)\le t\le t_p+\frac{1}{f_{rep}}(N-1) \\ \\ (e^{\alpha\lambda_{nm}^2 t_p}-1)e^{-\alpha\lambda_{nm}^2(t-\frac{1}{f_{rep}}(N-1))} & \text{in} \quad t_p+\frac{1}{f_{rep}}(N-1)<t<\frac{1}{f_{rep}}N \end{cases}
\end{aligned}
\tag{S33}
$$

S2 Thermo-elastic equation

Following Noda et al,[S3] the Navier's equations for axisymmetric thermoelastic problems without the body forces can be expressed as

$$
\bigtriangledown^2 u_z+\frac{1}{1-2v}\frac{\partial e}{\partial z}-2\alpha_z(\frac{1+v}{1-2v})\frac{\partial T}{\partial z}=0 \tag{S34}
$$

where

$$\bigtriangledown^2 = \frac{\partial^2}{\partial r^2} + \frac{1}{r}\frac{\partial}{\partial r} + \frac{\partial^2}{\partial z^2} \tag{S35}$$

where E Young's modulus, α_z coefficient of linear thermal expansion, v Poisson ratio. e is the dilatation defined by the sum of strain components

$$e = \epsilon_{xx} + \epsilon_{yy} + \epsilon_{zz} \tag{S36}$$

The solution of Naviers equations without body forces can be expressed by Goodiers thermoelastic displacement potential Φ and Boussinesq harmonic functions φ and ψ under the axisymmetric conditions.

$$u_z = \frac{\partial \Phi}{\partial z} + \frac{\partial \varphi}{\partial z} + z\frac{\partial \psi}{\partial z} - (3 - 4v)\psi \tag{S37}$$

in which the Goodiers thermoelastic displacement potential Φ must satisfy the governing equations

$$\bigtriangledown^2 \Phi = KT, \tag{S38}$$

where K is Restraint coefficient defined as[S3]

$$K = \frac{\beta}{\lambda + 2\mu} = (\frac{1+v}{1-v})\alpha_z \tag{S39}$$

where β is the thermoelastic constant, λ and μ are Lames elastic constants, α_z coefficient of the linear thermal expansion. Boussinesq harmonic functions φ and ψ must satisfy the governing equations

$$\bigtriangledown^2 \varphi = \frac{\partial^2 \varphi}{\partial r^2} + \frac{1}{r}\frac{\partial \varphi}{\partial r} + \frac{\partial^2 \varphi}{\partial z^2} = 0 \tag{S40}$$

$$\nabla^2\psi = \frac{\partial^2\psi}{\partial r^2} + \frac{1}{r}\frac{\partial\psi}{\partial r} + \frac{\partial^2\psi}{\partial z^2} = 0 \tag{S41}$$

The components of the stress are represented by the Goodier thermoelastic displacement potential Φ and Boussinesq harmonic functions φ, ψ are:

$$\sigma_{rr} = 2G\left(\frac{\partial^2\Phi}{\partial r^2} - KT + \frac{\partial^2\varphi}{\partial r^2} + z\frac{\partial^2\psi}{\partial r^2} - 2v\frac{\partial\psi}{\partial z}\right) \tag{S42}$$

$$\sigma_{\theta\theta} = 2G\left(\frac{1}{r}\frac{\partial\Phi}{\partial r} - KT + \frac{1}{r}\frac{\partial\varphi}{\partial r} + \frac{z}{r}\frac{\partial\psi}{\partial r} - 2v\frac{\partial\psi}{\partial z}\right) \tag{S43}$$

$$\sigma_{zz} = 2G\left[\frac{\partial^2\Phi}{\partial z^2} - KT + \frac{\partial^2\varphi}{\partial z^2} + z\frac{\partial^2\psi}{\partial z^2} - 2(1-v)\frac{\partial\psi}{\partial z}\right] \tag{S44}$$

$$\sigma_{zr} = 2G\left[\frac{\partial^2\Phi}{\partial r\partial z} + \frac{\partial^2\varphi}{\partial r\partial z} + z\frac{\partial^2\psi}{\partial r\partial z} - (1-2v)\frac{\partial\psi}{\partial r}\right] \tag{S45}$$

Referring to Eq.S41 and S40, the functions φ and ψ can be expressed by use of integrals satisfying the solution form as shown on[S3] under the axial symmetric condition,

$$\varphi = \sum_{n=0}^{\infty}\sum_{m=0}^{\infty} BJ_0(\beta_m r)e^{-\beta_m z} \tag{S46}$$

$$\psi = \sum_{n=0}^{\infty}\sum_{m=0}^{\infty} CJ_0(\beta_m r)e^{-\beta_m z} \tag{S47}$$

The Goodier thermoelastic displacement potential Φ can be expressed as,

$$\Phi(r,z,t) = \sum_{n=0}^{\infty}\sum_{m=0}^{\infty} \frac{-A(\beta_m,\eta_n)K}{\beta_m^2+\eta_n^2} J_0(\beta_m r) sin(\eta_n z)\mathcal{T}(t) \tag{S48}$$

Substituting Eq.S46, S47 and S48 into S37, the displacement is

$$\begin{aligned} u_z(r,z,t)) = \sum_{n=0}^{\infty}\sum_{m=0}^{\infty}\Bigg[& \frac{-A(\beta_m,\eta_n)K\eta_n}{\beta_m^2+\eta_n^2} J_0(\beta_m r) cos(\eta_n z)\mathcal{T}(t) \\ & + ((B+zC)\beta_m - (3-4v)C) J_0(\beta_m r) e^{-\beta_m z}\Bigg] \end{aligned} \tag{S49}$$

The boundary conditions on the traction free surface are

$$\sigma_{zz} = 0, \quad \sigma_{zr} = 0 \quad on \quad z = h_{mat} \tag{S50}$$

The unknown functions B and C can be determined from the boundary conditions S50

$$C = \frac{A(\beta_m,\eta_n)K}{\beta_m e^{-\beta_m L}} (\frac{\eta_n^2}{\beta_m^2+\eta_n^2} + 1)\mathcal{T}(t) \tag{S51}$$

$$B = -\frac{1-2v+L\beta_m}{\beta_m} C \tag{S52}$$

Substituting Eq.S52 and S51 into Eq. S49, the displacements at surface can be simplified as,

$$u_z(r,h_{mat},t) = \sum_{n=0}^{\infty}\sum_{m=0}^{\infty} \frac{2(v-1)A(\beta_m,\eta_n)K}{\beta_m} (\frac{\eta_n^2}{\beta_m^2+\eta_n^2} + 1) J_0(\beta_m r)\mathcal{T}(t) \tag{S53}$$

S3 Material Properties

Table 1: Parameters used in finite-difference time domain model and PSF model of AFM-IR simulations. The thermal, mechanical and thermo-mechanical properties listed below.

Property*	PMMA	PE	air	silicon
absorption coefficient (1/cm)	960[S4]	-	-	-
coefficient of thermal expansion (1/k)	193.6×10^{-6} [S5]	150×10^{-6} [S6]	-	2.6×10^{-6} [S7]
thermal conductivity (W/(m· k))	0.192[S8]	0.25[S9]	0.025[S10]	130[S7]
density (kg/m^3)	1190[S11]	930[S12]	1.2[S10]	2329[S7]
heat capacity (J/(kg·k))	1420[S13]	1900[S14]	1015[S10]	700[S7]
Young's modulus (GPa)	2.4[S15]	1[S12]	-	170[S16]
Poisson's ratio	0.37[S15]	0.46[S12]	-	0.28[S16]

*These values are treated as exact numbers for the purpose of simulations.

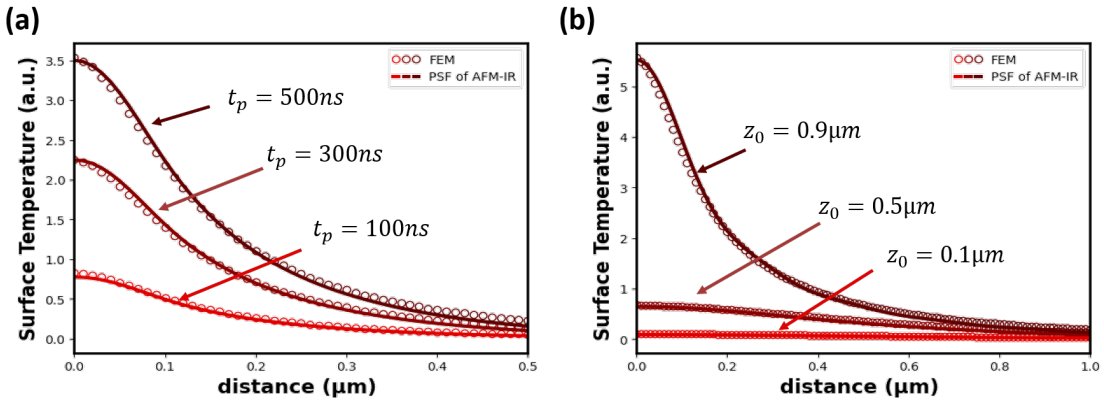

Figure S1: **Surface temperature for three different laser pulse widths and depth positions of the obsorber. (a)** Temperature profile is examined for three different pulse widths at a laser repetition rate of 500 kHz. The absorber is positioned at a depth of z_0 = 0.9 µm. **(b)** Temperature profile is examined for three different depth positions of the obsorber. At a laser repetition rate of 500 kHz and a pulse width of 100 ns.

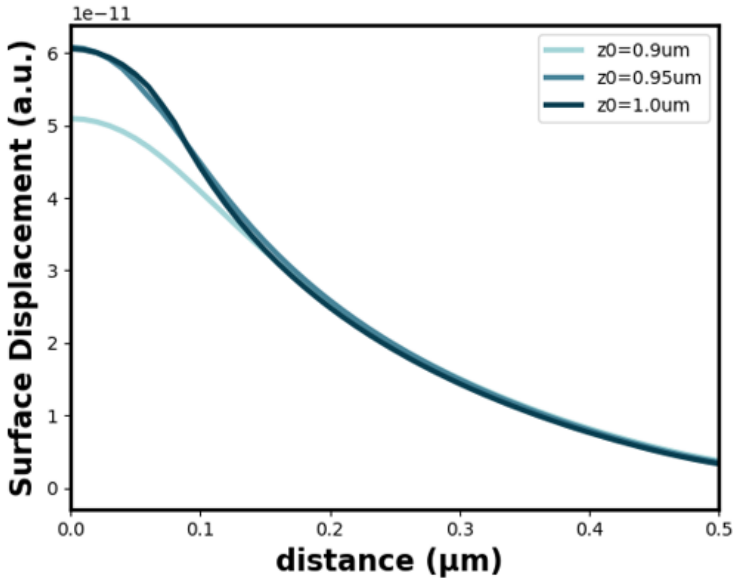

Figure S2: Thermo-elastic surface displacement profile are examined for three different depth positions of the obsorber. At a laser repetition rate of 500 kHz and a pulse width of 100 ns. When $z_0 = 0.95\,\mu$m, the PMMA bead is 20 nm outside of the surface .

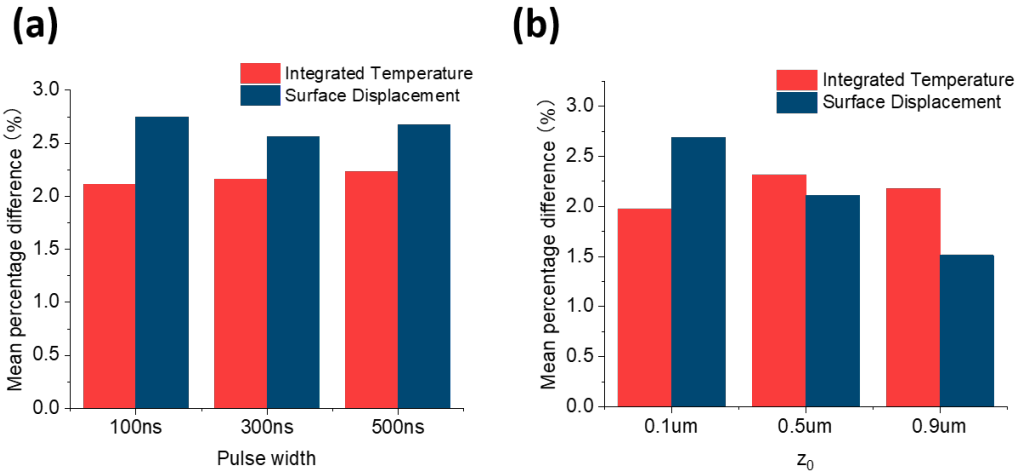

Figure S3: Mean percentage difference analysis of integrated temperature and displacement between PSF model of AFM-IR and FEM simulations at tested pulse widths and depth positions of the absorber.

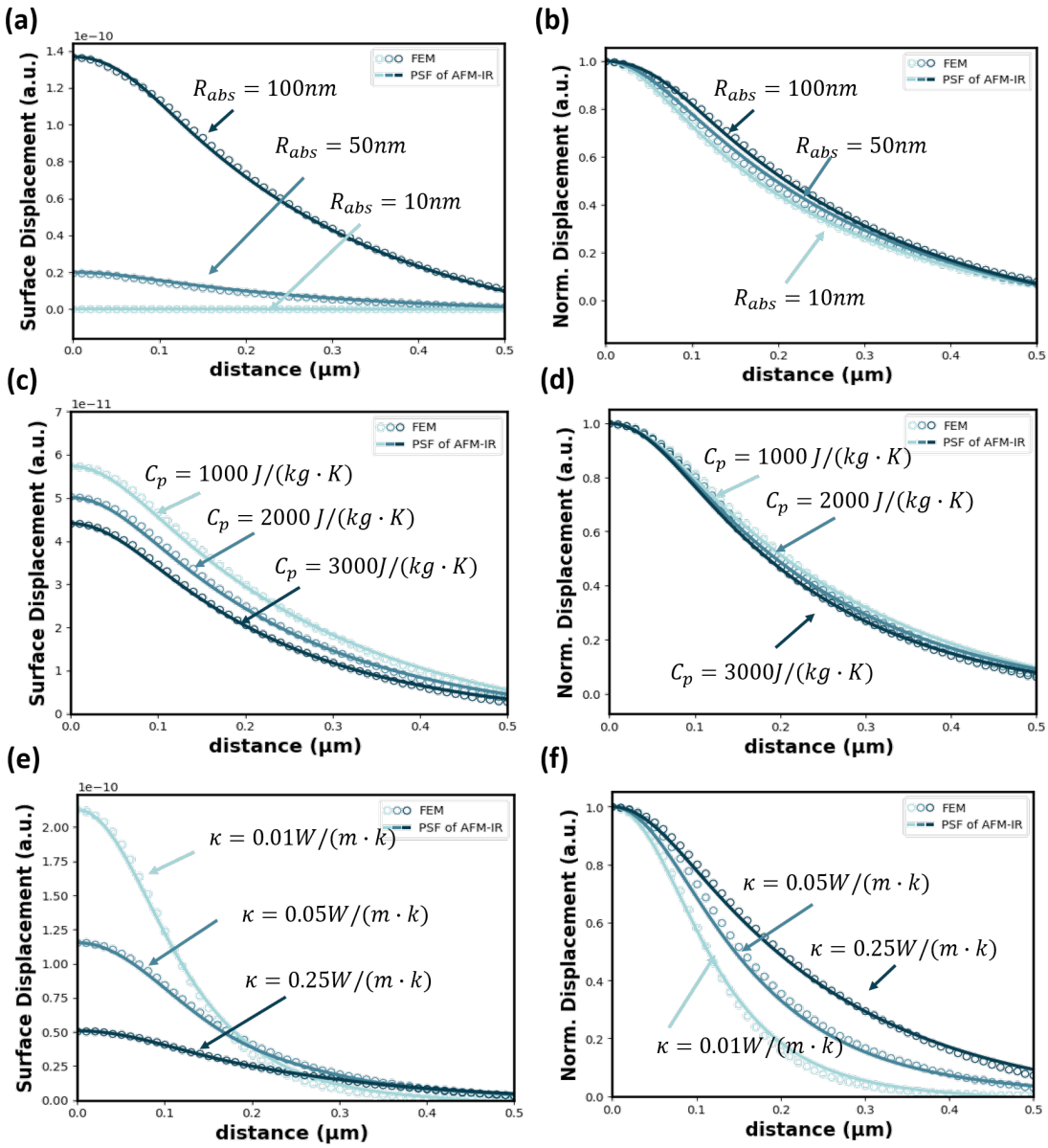

Figure S4: **Surface displacement profiles for different geometries and material properties.** **(a)** displacement profile are examined for three different sizes of the obsorber; **(b)** normalized displacement profile for absorbers in three different sizes; **(c)** displacement profile are examined for three different specific heat capacities of the matrix; **(b)** normalized displacement profile at three different specific heat capacity of the matrix; . **(e)** displacement profile are examined for three different thermal conductivity coefficients of the matrix; **(f)** normalized displacement profile at three different thermal conductivity coefficients of the matrix .

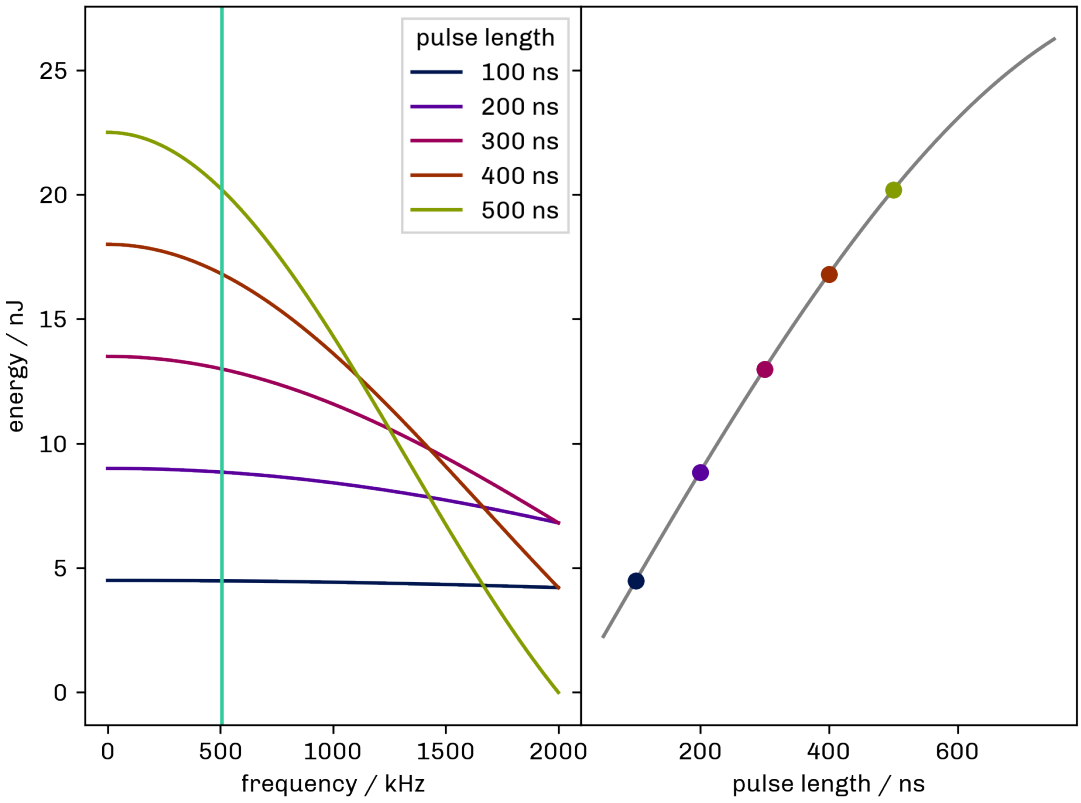

Figure S5: The left side exhibits the frequency domain characteristics of a rectangular function, whereas the right side illustrates the power pulse width function.

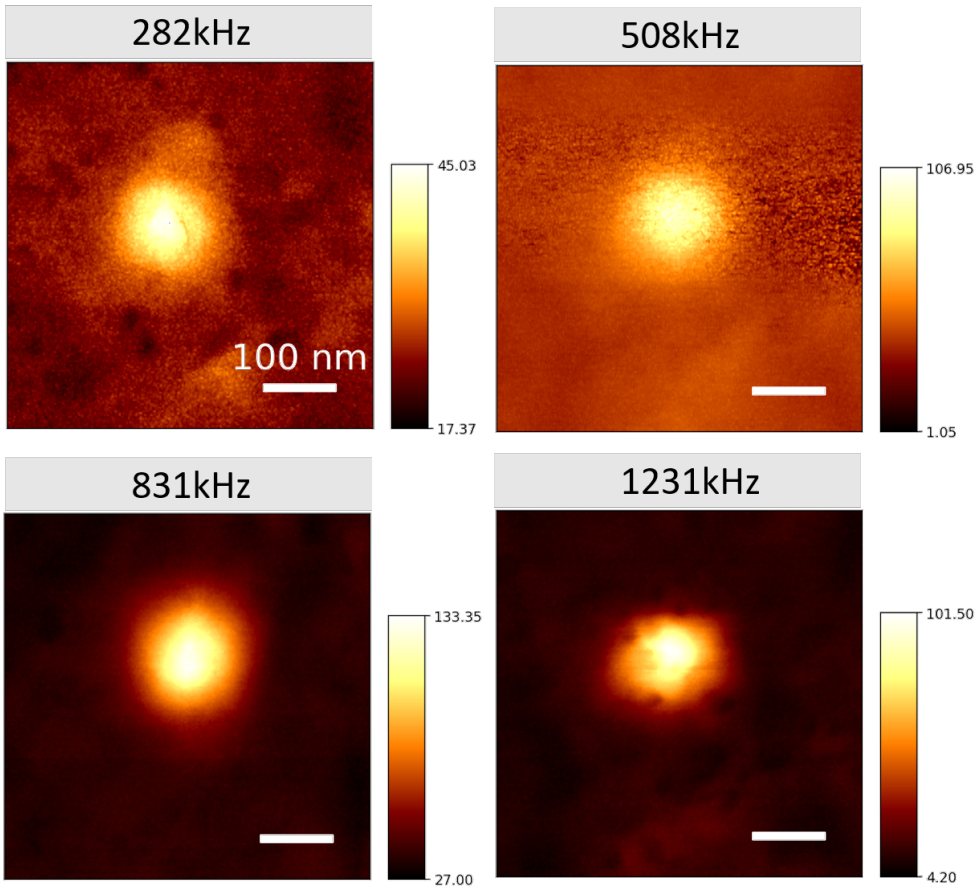

Figure S6: AFM-IR images were obtained for various laser repetition rates of 282 kHz, 508 kHz, 831 kHz, and 1231 kHz at a pulse width of 100 ns.

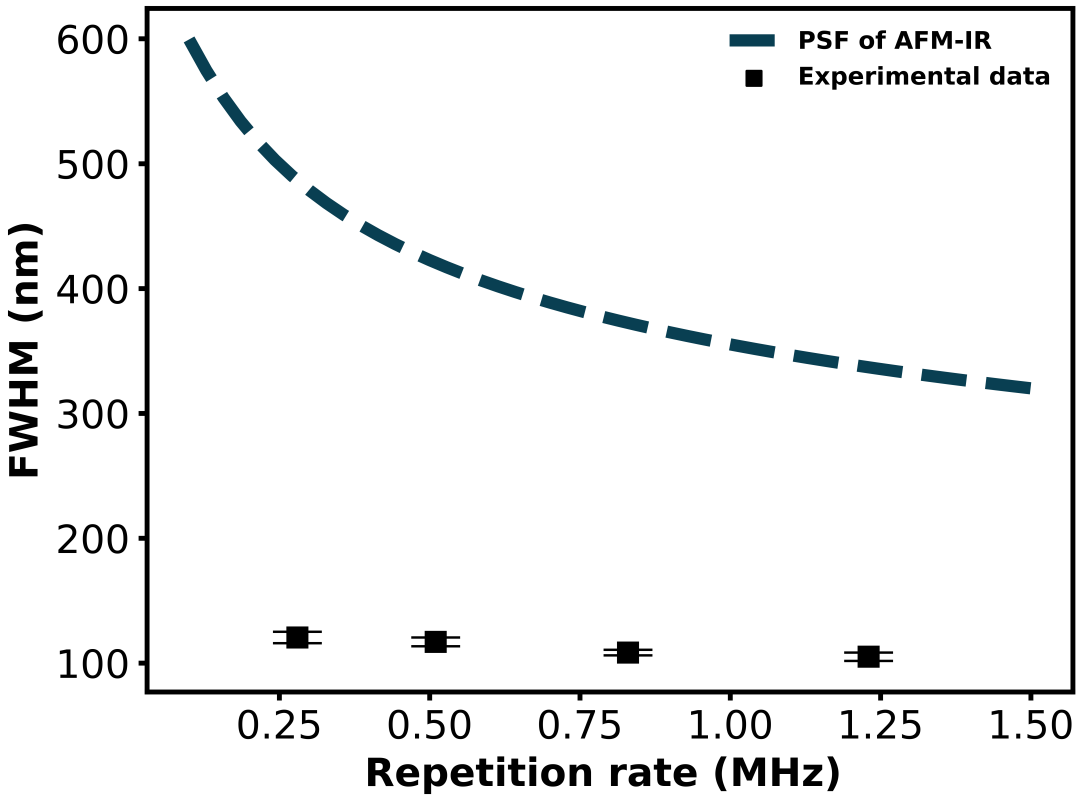

Figure S7: FWHM of AFM-IR signal cross section was measured at laser repetition rates of 282 kHz, 508 kHz, 831 kHz, and 1231 kHz. Simulated line from the PSF model, excluding the consideration of interfacial thermal resistance.

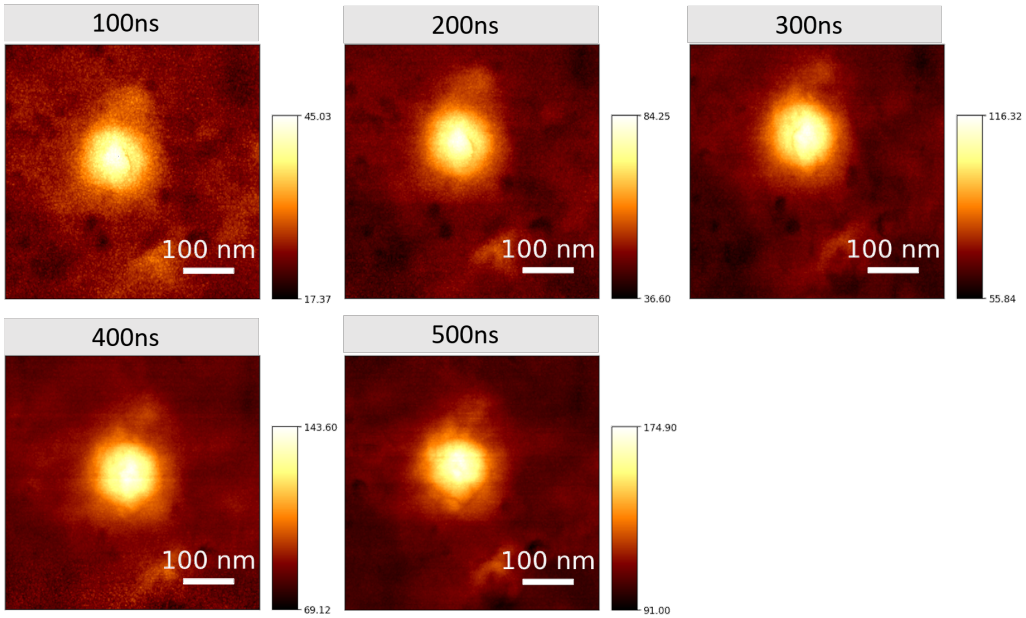

Figure S8: Experimental AFM-IR images were obtained using a series of laser pulse widths ranging from 100 ns to 500 ns at a laser repetition rate of 282 kHz.

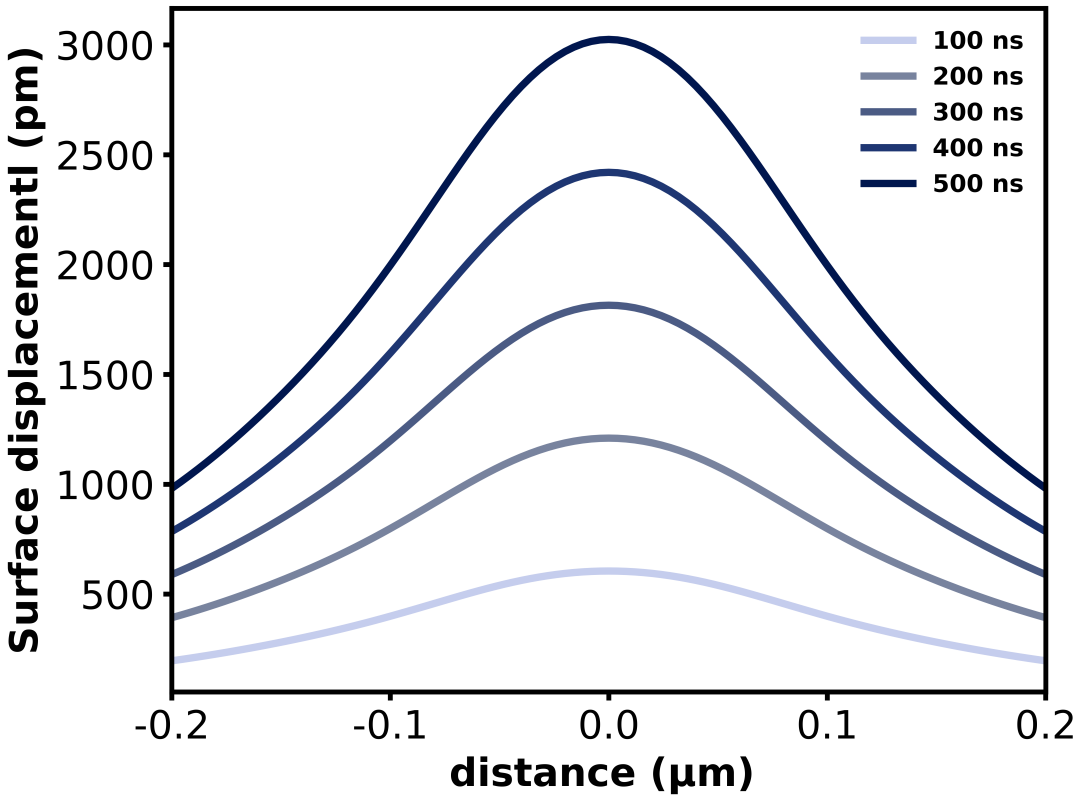

Figure S9: Simulated surface displacement profiles at different pulse widths based on PSF model of AFM-IR. Considering laser power 4.5 mW, beam diameter $r_{laser} = 10\,\mu m$, diameter of 140 nm for the absorber, positioned at a depth of 0.93 µm, tightly under the surface.

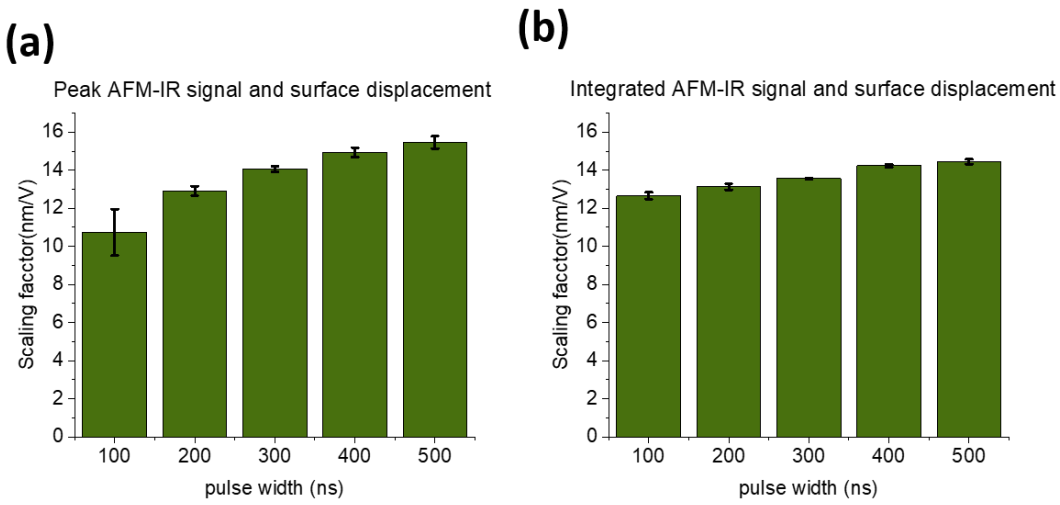

Figure S10: Calculated scaling factors for surface displacement and AFM-IR signal at different pulse widths ranging from 100 ns to 500 ns. (a) Peak AFM-IR signal and surface displacement. (b) Integrated AFM-IR signal and surface displacement.

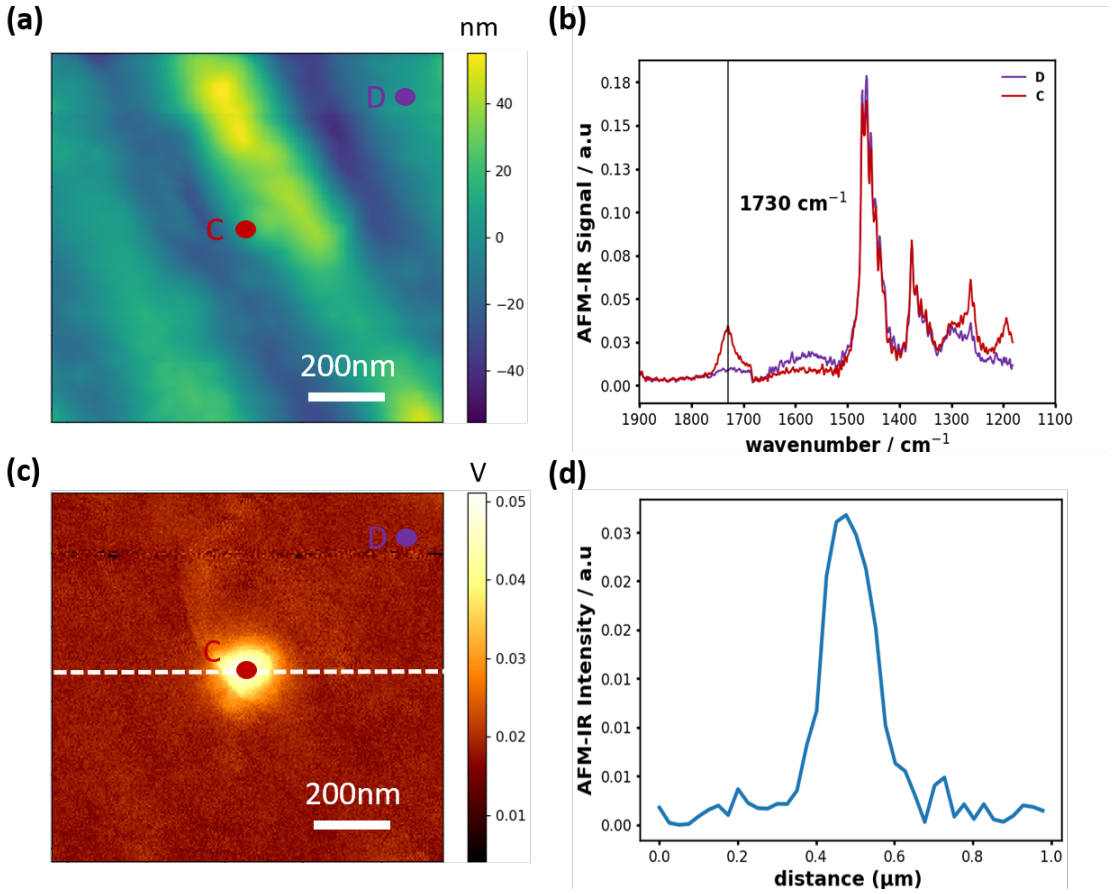

Figure S11: Measurement of another PMMA bead, showcasing further examples and insights into the behavior and characteristics of the PMMA beads in the study. PMMA bead measurement under condition of laser repetition rate 287 kHz, pulse length 100 ns. **(a)** AFM topography image of a PMMA nanoparticle. **(b)** AFM-IR spectra obtained on the position C and D, respectively. **(c)** Corresponding AFM-IR chemical map at 1730 cm^{-1}. The dashed line corresponds to the profile in (d). **(d)** Cross section profile of the AFM-IR signal distribution.

S4 Fluorescence microscopy

Taking advantage of the carboxylated surface modification of the PMMA nano-beads (Excitation wavelengths: 450-565nm; Emission wavelengths: 540-620nm), fluorescence microscopy is enabled. This not only allows us the registration of the location of interest for the following AFM-IR measurements, but also enables fluorescence stacking images to get a first idea of the sample composition (see Fig. S12). These measurements were carried out using a WiTec alpha300 R Confocal Microscope (WiTec GmbH).

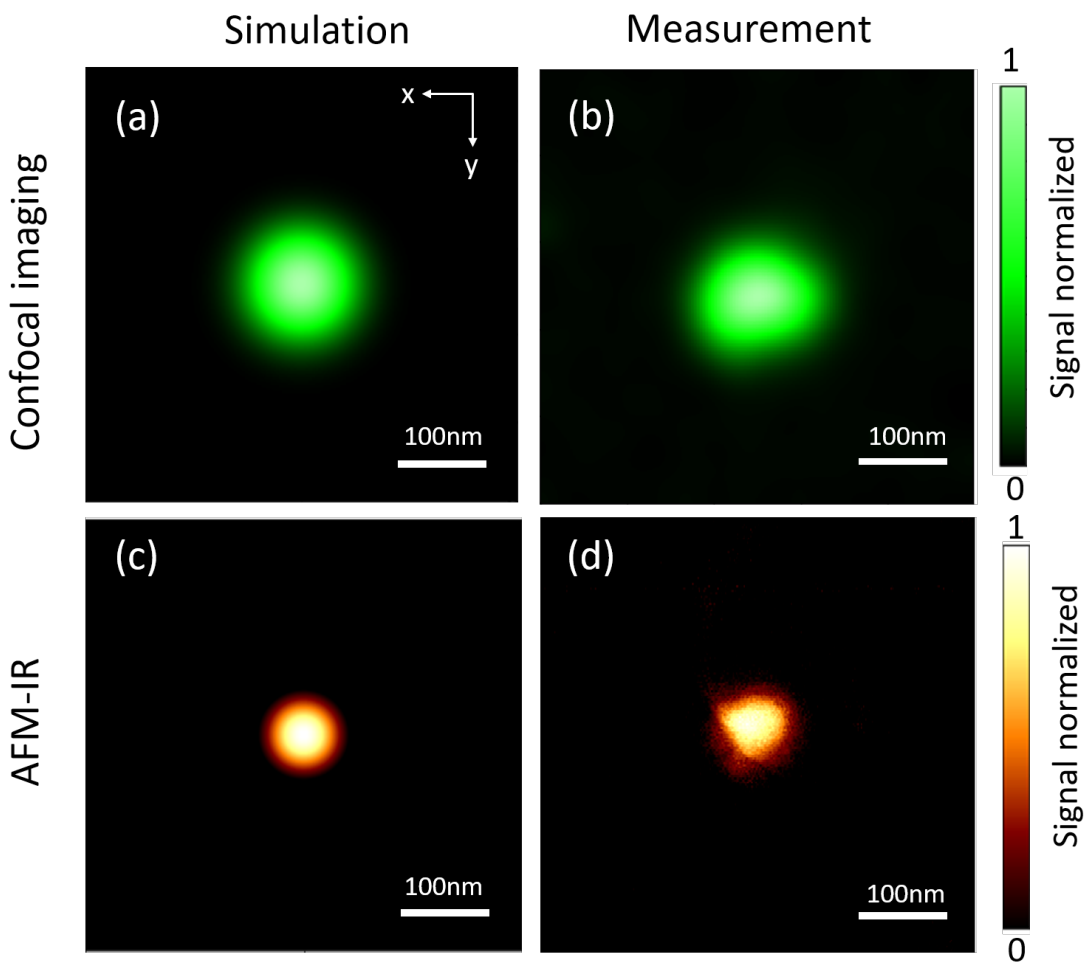

Figure S12: Comparison of simulated confocal imaging with AFM-IR chemical mapping. (a) Simulated PSF of confocal imaging at N.A. 0.9 and 540 nm emission wavelength. (b) Measured confocal fluorescence imaging of single PMMA bead. (c) Simulated 140 nm diameter size absorber in the center of the sample based on PSF of AFM-IR with 100 ns laser pulse width and 287 kHz repetition rate. (d) Measured AFM-IR chemical imaging at wavenumber 1730 cm^{-1} with 100 ns laser pulse width and 287 kHz repetition rate.

References

[S1] Cole, K. D., Ed. *Heat conduction using Green's functions*, 2nd ed.; Series in Computational and Physical Processes in Mechanics and Thermal Sciences; CRC Press: Boca Raton, 2011.

[S2] Hahn, D. W.; Özişik, M. N. *Heat conduction*, 3rd ed.; Wiley: Hoboken, NJ, 2012.

[S3] Noda, N.; Hetnarski, R. B.; Tanigawa, Y. *Thermal stresses*, 2nd ed.; Taylor & Francis: New York, 2003.

[S4] Faria, L.; Moreira, R. L. Infrared spectroscopic investigation of chain conformations and interactions in P(VDF-TrFE)/PMMA blends. *Journal of Polymer Science Part B: Polymer Physics* **2000**, *38*, 34–40.

[S5] Wang, J.; Lee, M. K.; Park, S.-M.; Hong, S.; Kim, N. A study on the mechanical properties and deformation behavior of injection molded PMMA-TSP laminated composite. *Korea-Australia Rheology Journal* **2012**, *24*, 23–33.

[S6] Yang, H.-S.; Wolcott, M. P.; Kim, H.-S.; Kim, H.-J. Thermal properties of lignocellulosic filler-thermoplastic polymer bio-composites. *Journal of Thermal Analysis and Calorimetry* **2005**, *82*, 157–160.

[S7] Henins, I. Precision density measurement of silicon. *Journal of Research of the National Bureau of Standards Section A: Physics and Chemistry* **1964**, *68A*, 529.

[S8] Assael, M. J.; Botsios, S.; Gialou, K.; Metaxa, I. N. Thermal Conductivity of Polymethyl Methacrylate (PMMA) and Borosilicate Crown Glass BK7. *International Journal of Thermophysics* **2005**, *26*, 1595–1605.

[S9] Sheldon, R.; Lane, S. K. Thermal conductivities of polymers II—Polyethylene. *Polymer* **1965**, *6*, 205–212.

[S10] Kadoya, K.; Matsunaga, N.; Nagashima, A. Viscosity and Thermal Conductivity of Dry Air in the Gaseous Phase. *Journal of Physical and Chemical Reference Data* **1985**, *14*, 947–970.

[S11] Gaur, U.; Lau, S.-f.; Wunderlich, B. B.; Wunderlich, B. Heat Capacity and Other Thermodynamic Properties of Linear Macromolecules VI. Acrylic Polymers. *Journal of Physical and Chemical Reference Data* **1982**, *11*, 1065–1089.

[S12] Jordan, J. L.; Rowland, R. L.; Greenhall, J.; Moss, E. K.; Huber, R. C.; Willis, E. C.; Hrubiak, R.; Kenney-Benson, C.; Bartram, B.; Sturtevant, B. T. Elastic properties of polyethylene from high pressure sound speed measurements. *Polymer* **2021**, *212*, 123164.

[S13] Nogueira, T.; Botan, R.; Wypych, F.; Lona, L. Study of thermal and mechanical properties of PMMA/LDHs nanocomposites obtained by in situ bulk polymerization. *Composites Part A: Applied Science and Manufacturing* **2011**, *42*, 1025–1030.

[S14] Salameh, B.; Yasin, S.; Fara, D. A.; Zihlif, A. M. Dependence of the Thermal Conductivity of PMMA, PS and PE on Temperature and Crystallinity. *Polymer Korea* **2021**, *45*, 281–285.

[S15] Li, K.; Xu, G.; Huang, X.; Xie, Z.; Gong, F. Manufacturing of Micro-Lens Array Using Contactless Micro-Embossing with an EDM-Mold. *Applied Sciences* **2018**, *9*, 85.

[S16] Hopcroft, M. A.; Nix, W. D.; Kenny, T. W. What is the Young's Modulus of Silicon? *Journal of Microelectromechanical Systems* **2010**, *19*, 229–238.